JOURNAL OF AIRCRAFT
Vol. 31, No. 3, May–June 1994

Computational Study of the F-5A Forebody Emphasizing Directional Stability

William H. Mason* and R. Ravi†
Virginia Polytechnic Institute and State University, Blacksburg, Virginia 24061

Computational fluid dynamics (CFD) has been used to study the F-5A forebody flowfield at low-speed high angle-of-attack conditions combined with sideslip. The classic wind-tunnel experiment demonstrating the dominant contribution of the F-5A forebody to directional stability at high angle of attack has been simulated computationally over an angle-of-attack range from 10 to 45 deg. The key wind-tunnel trend for $C_{n\beta}$ was obtained computationally using the CFL3D code to solve the Reynolds' equations employing the Baldwin-Lomax turbulence model with the Degani-Schiff modification to account for massive crossflow separation. The computations provide detailed and fascinating insights into the physics of flowfield. The results of the investigation show that CFD has reached a level of development where computational methods can be used for high angle-of-attack aerodynamic design.

Nomenclature

b' = wingspan based on F-5A wind-tunnel model, 52.68 in.
C_L = lift coefficient, lift/$q_\infty S_{\text{ref}}$
C_m = pitching-moment coefficient, pitching moment/$q_\infty S_{\text{ref}} b'$
C_n = yawing-moment coefficient, yawing moment/$q_\infty S_{\text{ref}} b'$
$C_{n\beta}$ = directional stability derivative, $\partial C_n/\partial\beta$
C_p = pressure coefficient, $(p - p_\infty)/q_\infty$
C_y = side-force coefficient, side force/$q_\infty S_{\text{ref}}$
c = mean aerodynamic chord, 16.08 in.
c_y = sectional side force, section side force/q_∞
FS = fuselage station
l = forebody model length, 31.025 in.
M_∞ = freestream Mach number, 0.2
p = pressure
p_∞ = freestream pressure
q_∞ = freestream dynamic pressure
Re_l = Reynolds number based on model length, 1.25×10^6
S_{ref} = reference area, 754.56 in.^{2}
u^* = wall friction velocity, $\sqrt{\tau_w/\rho}$
V_{sep} = crossflow velocity magnitude at separation point (chine edge)
x, y, z = coordinate system: x positive aft on model axis, y positive to right, and z positive up
y^+ = inner law variable, yu^*/ν
α = angle of attack, deg
β = angle of sideslip, deg
ΔC_p = difference between leeward and windward C_p across the vertical plane of symmetry
θ = azimuthal angle, measured clockwise from windward plane at any cross section
ρ = density
τ_w = shear stress at the wall

Presented as Paper 91-3289 at the AIAA 9th Applied Aerodynamics Conference, Baltimore, MD, Sept. 23–25, 1991; received June 18, 1992; revision received Nov. 7, 1992; accepted for publication Nov. 9, 1992.

*Associate Professor, Department of Aerospace and Ocean Engineering. Associate Fellow AIAA.
†Graduate Research Assistant, Department of Aerospace and Ocean Engineering. Student Member AIAA.

Introduction

HIGH angle-of-attack aerodynamic characteristics of advanced fighter aircraft are an important part of the configuration development. High angle-of-attack aerodynamic design is currently conducted primarily in wind tunnels, and the high angle-of-attack characteristics of the forebody are a significant part of this design work. The specific characteristics of interest associated with the forebody flowfield include flow asymmetries, advanced control device concepts (e.g., forebody "flaps"), yaw damping, and directional stability.[1–3] The requirement for advanced control devices and control systems is in large part due to directional stability characteristics. If the basic directional stability characteristics can be aerodynamically tailored by shaping the forebody, demands on control systems and control devices can be dramatically decreased, and complicated forebody mechanisms (which are undesirable from an aircraft designer's point of view) may not be required.

The F-5A has demonstrated good high angle-of-attack characteristics[2] and has been studied experimentally in detail. Figure 1 replots data from the report by Grafton et al.[4] The figure shows that at low angle of attack, the vertical tail provides directional stability. As the angle of attack increases, the tail loses effectiveness because of its location in the separated flow region behind the fuselage and wing. The figure also shows that the directional stability increases again as the angle of attack increases further. The directional stability obtained from a wind-tunnel test of the isolated forebody is also shown. In this case, the directional stability of the forebody alone is nearly identical to the directional stability of the entire aircraft above $\alpha = 30$ deg. This classic data is often used to show the dominant role played by the forebody in determining the directional stability at high angle of attack for an F-5A-type configuration. The inset in Fig. 1 shows the isolated forebody test setup and the hypothesized flow model, where the stronger and more closely located to the body leeward vortex provides a net restoring force (positive stability) on the forebody.

The capability now exists to use computational fluid dynamics (CFD) to investigate the design of aircraft components at high angle of attack. This has been demonstrated by recent computational results, where one example is the analysis of the F/A-18 by Ghaffari et al.[5] Calculations have also been made for tangent-ogives, including the effects of surface perturbations on flow asymmetry.[6–8] However, none of the previous work has examined the ability of CFD methods to compute side forces arising from combined angle of attack and

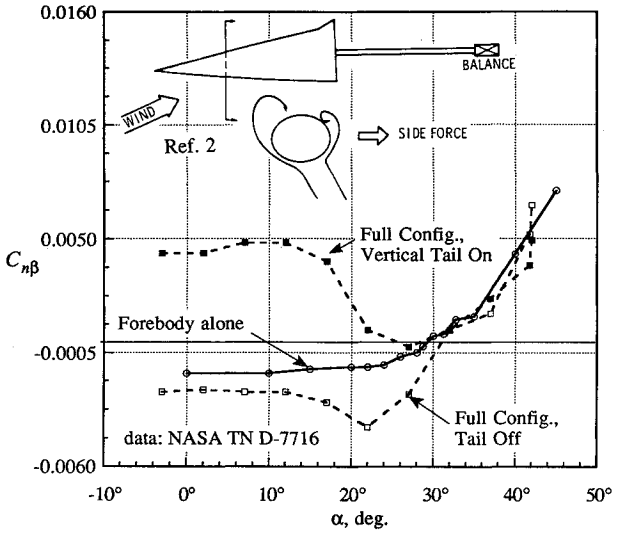

Fig. 1 Directional stability characteristics of the F-5A aircraft and its forebody alone, with the hypothesized flow model shown.

sideslip on nonaxisymmetric forebodies. If the codes can be used to predict the sideforce, and hence, yawing moment and directional stability, then they can be used to try to design forebodies to achieve desired aerodynamic characteristics.

This article provides the results of an analysis of the F-5A forebody conducted to determine if a current, widely used CFD code, CFL3D,[9] could be used to 1) reproduce the experimental results obtained by Grafton et al.,[4] and 2) use the detailed flowfield information available from the computational simulation to gain insight into the flowfield mechanism responsible for the positive contribution to directional stability provided by this forebody at high angle of attack. A discussion of the results is preceded by a description of the use of CFL3D in a combined α/β flowfield and the development of the forebody geometry and computational grid.

Governing Equations and Computational Approach

The baseline code for this work was the NASA Langley program CFL3D.[9] This code solves the three-dimensional time-dependent conservation law form of the compressible Euler and thin-layer Navier-Stokes (or Reynolds-averaged) equations. An implicit time advancement algorithm is used, including acceleration to steady-state solutions. Steady-state solutions were obtained and are discussed in this article.

For turbulent flow, CFL3D uses the Reynolds-averaged counterparts of the Navier-Stokes equations. An algebraic turbulence model is used, where the turbulent viscosity is obtained using the two-layer algebraic eddy viscosity of Baldwin and Lomax.[10] For separated flow regions, the code employs the modification to this model suggested by Degani and Schiff.[11-13] At high angles of attack, in regions of massive crossflow separation, the Baldwin-Lomax model picks a turbulent length scale based on the distance to the free shear layer which overpredicts the value of the eddy viscosity. The Degani-Schiff modification allows the code to choose a more appropriate length scale based on the attached flow boundary layer below the primary and secondary vortices.

In the present computations, the convective and pressure terms arising in the flux quantities are represented using a third-order upwind-biased algorithm with the flux-difference-splitting approach of Roe.[14] The code can handle multiple blocks, and when used, information is exchanged between the computational blocks using the patching algorithm described by Thomas et al.[15]

The far-field computational boundaries were located sufficiently far away from the body so as not to affect the forces on the body. They were chosen to be consistent with those used by other investigators, e.g., analysis of an F/A-18[5] and tangent-ogive.[6] The exact distances are given with the description of the computational grid, and were established after computational experiments on an equivalent tangent-ogive. Inflow-outflow boundary conditions were used at the far-field inflow, far-field outflow, and the far-field outer boundary. For turbulent computations, the grid ahead of the nose was treated as a separate block (as described below). When viscous effects are included, the no-slip as well as nonpenetration conditions are enforced on the body. At the plane of geometric symmetry, periodic conditions are used to include sideslip as well as angle of attack in the freestream flow.

Some initial startup activity was required before beginning the study. The code was modified to handle the boundary conditions for combined α/β flows, and then validated for operation at combined angles of α and β. The validation of our use of the code was done by computing the tangent-ogive case studied previously by Hartwich and Hall,[6] and checking that the results obtained agreed with their published results. To verify the sideslip capability, the code was used to compute the flowfield and forces for both $\alpha = 20$ deg, $\beta = 0$ deg and $\alpha = 0$ deg, $\beta = 20$ deg. The surface pressure results agreed exactly when one case was shifted by 90 deg. The forces were found to correspond, e.g., the lift for the $\alpha = 20$ deg, $\beta = 0$-deg case was equal to the side force for the $\alpha = 0$ deg, $\beta = 20$-deg case.

The computations were made on the NASA Langley Cray-2S computer. Analysis of the flowfield calculations was carried out for the more complicated aspects of the grid and flow visualization using the NASA Ames code PLOT3D.[16]

F-5A Forebody Geometry Math Model

The computational math model of the surface was constructed using classical conic lofting techniques[17] based on the lofting information provided by Northrop. The configuration was modeled from the nose longitudinally back to $x = 225$ in. (in full scale). The computational model (which was constructed in the wind-tunnel model scale) did not include the canopy. One interesting complication arose. At sections close to the nose, the upper and the lower maximum half-breadth points coincide. However, at sections downstream the upper and lower maximum, half-breadth points are separated by a flat sidewall.

To verify that the wind-tunnel model geometry agreed with the math model, NASA Langley provided the forebody from the wind-tunnel model of the F-5A. The model was a 0.17-scale model of the full-scale airplane. Figure 2 shows the wind-tunnel model forebody and the setup that was used to make templates of the cross sections. The measured shape of the forebody at different cross sections was then digitized from a

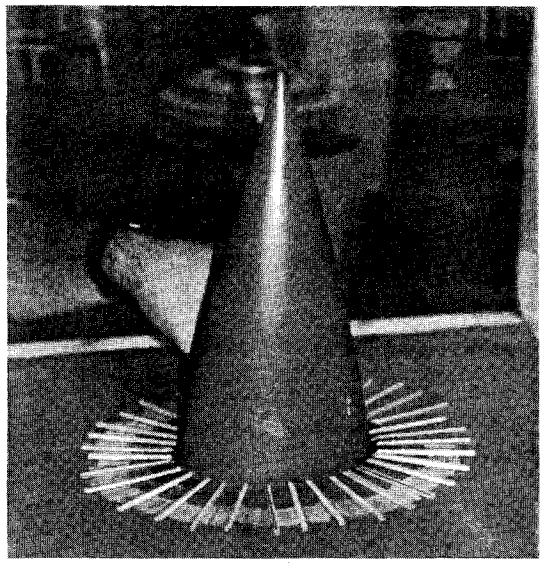

Fig. 2 F-5A wind-tunnel model forebody inspection.

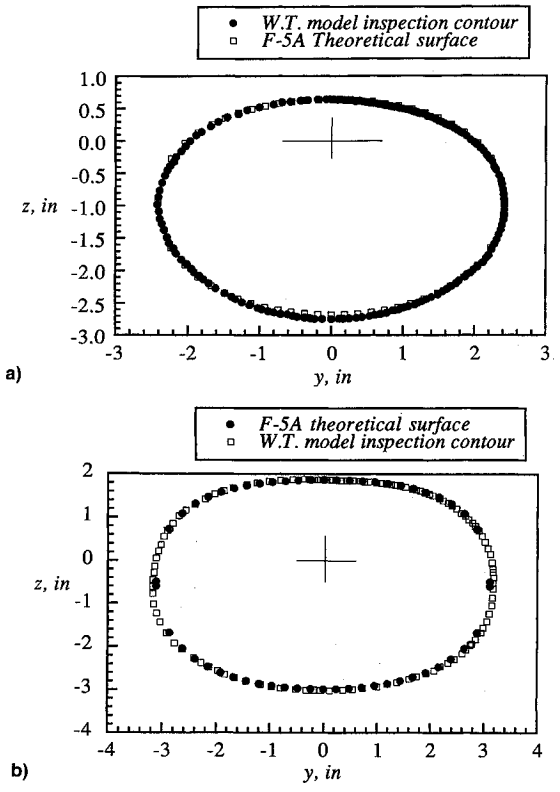

Fig. 3 Validation of F-5A math model. Comparison of math model and WT model: a) FS 9.1875 and b) FS 15.3125.

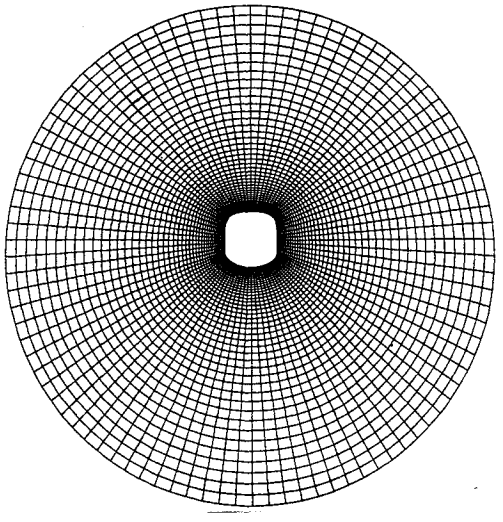

Fig. 4 Grid details in crossflow plane at FS 29.61.

tracing of the shape defined by the template, and compared with the computational model. The cross-sectional shapes of the computational and wind-tunnel models agree very well, considering the method used to obtain the model shape. The comparison is shown in Figs. 3a and 3b.

Computational Grid

The initial three-dimensional grid was constructed from two-dimensional O-type crossflow grids which are longitudinally stacked, constituting an H-O topology. The two-dimensional grid in the cross plane was generated using a grid generator provided by McGrory[18] that was originally developed to construct the grid for the calculation of the SR-71 flowfield.[19] The boundaries upstream of the nose, and radially away, were initially selected to be consistent with the F/A-18 calculations.[5] The forward boundary extends upstream of the nose by $0.62l$, and radial outer boundary extends $0.98l$ from the model centerline (8.4 equivalent body radii). The reference length l is

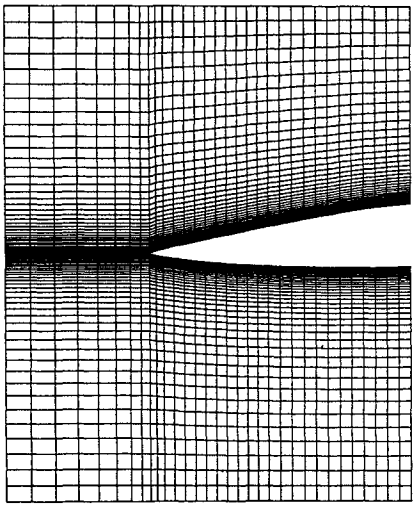

Fig. 5 Stacked H-O grid topology used for computations.

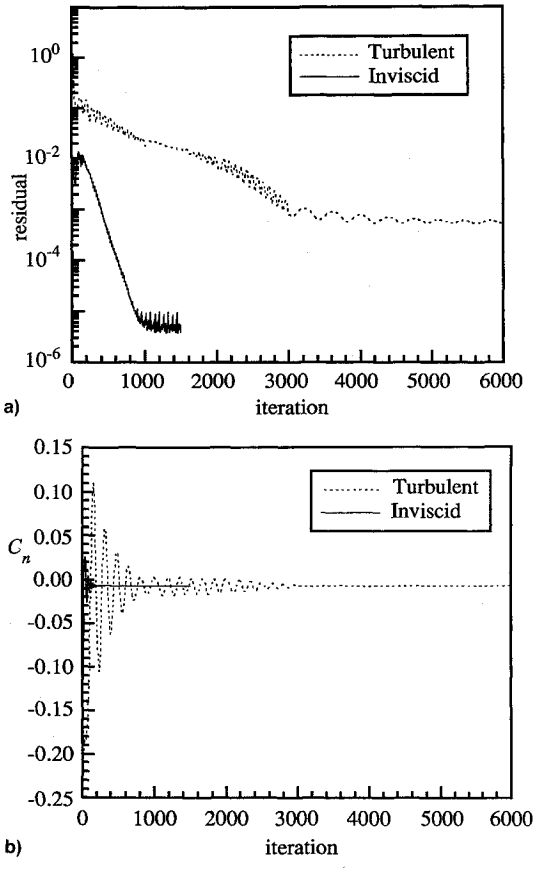

Fig. 6 Solution convergence history: a) residual history and b) yawing moment history.

equal to the longitudinal extent of the forebody, which was 31.025 in. using the wind-tunnel model scale. Preliminary calculations showed these to be sufficiently far away from the body so as not to affect the forces and moments on the body.

For inviscid calculations, the baseline grid had 45 points in the radial direction and 93 points in the full circumferential direction. Longitudinally, the grid was clustered near the nose with 25 stations on the forebody and 8 stations ahead of the nose. The grid upstream of the nose was also longitudinally stretched to provide resolution near the nose. The entire inviscid baseline grid consisted of 138,105 points.

For viscous calculations, the baseline grid had 65 points in the radial direction with longitudinal and circumferential grid points remaining the same as used for the inviscid calculations. The total number of grid points for the viscous grid was 199,485 points. The grid upstream of the nose was treated as a separate

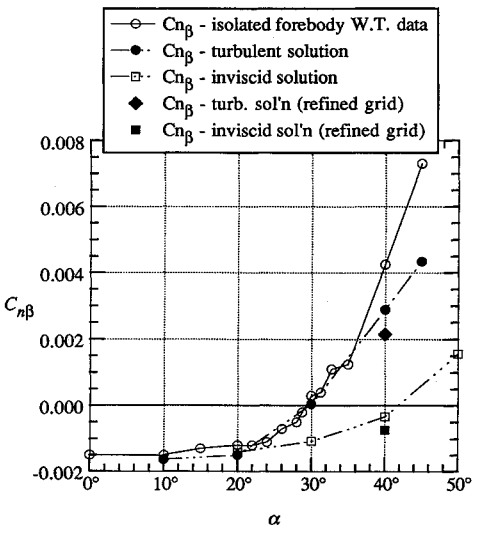

Fig. 7 Comparison of experimental and computed directional stability for the F-5A.

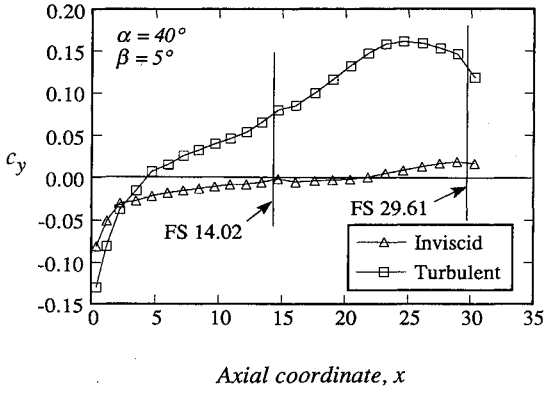

Fig. 8 Distribution of side force along forebody.

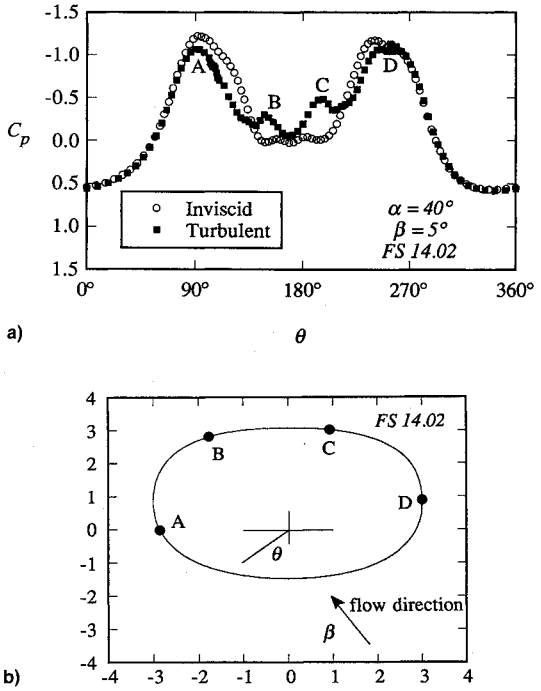

Fig. 9 F-5A surface pressure at cross section FS 14.02: a) inviscid and turbulent surface pressure distribution and b) cross section at FS 14.02.

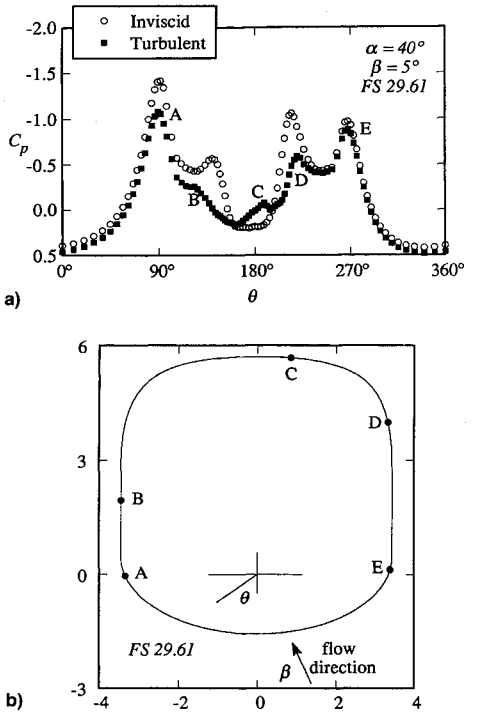

Fig. 10 F-5A surface pressure at cross section FS 29.61: a) inviscid and turbulent surface pressure distribution and b) cross section at FS 29.61.

block for turbulent flow calculations. Figure 4 shows the entire crossflow grid at FS 29.61 used for the viscous calculations. Because of the presence of the flat sidewall at sections downstream, as described earlier, the grid points were clustered near the maximum half-breadth points forward of the flat sidewall. This provided adequate definition on the flat wall portion of the forebody and created smoothly varying longitudinal grid lines. Figure 5 shows the longitudinal grid on the plane of symmetry and demonstrates the stretching of the grids.

For viscous calculations, the grid was established with sufficient normal clustering near the surface to adequately resolve the laminar sublayer for the turbulent boundary-layer flow. This grid produced an average normal cell size of approximately $10^{-4}l$. At the computational freestream conditions ($M_\infty = 0.2$, $Re_l = 1.25 \times 10^6$), the baseline grid typically resulted in a value of $y^+ \approx 2$ at the first mesh point away from the body.

It is difficult using an H-O grid topology to resolve the flow details near the nose. Hence, an alternate two-block grid was investigated, where the first block used a C-O topology to improve the resolution at the nose. Results obtained using this grid verified the H-O grid results. The C-O grid is presented in Ref. 20. Except very close to the nose, the results were identical. Thus, all the results presented in this article were computed using the H-O grid topology.

A grid refinement study was done for both the inviscid and viscous solutions on the H-O grid for $\alpha = 40$ deg. In either case, the number of points in the radial direction were increased with improved radial stretching, so that at least four fine grid points were present in the first grid point of the crude grid. The circumferential and axial density were kept the same. The inviscid refined grid had 90 points in the radial direction while the viscous refined grid had 100 points.

Results and Discussion

Inviscid calculations were performed for $\alpha = 20$, 30, 40, and 50 deg, with sideslip angles of $\beta = 0$, 5, and 10 deg. Turbulent calculations were performed for $\alpha = 10$, 20, 30, 40, and 45 deg, and $\beta = 5$ deg. Results at $\beta = 0$ deg produced symmetrical flowfields, $C_n = 0$, and were not needed to find

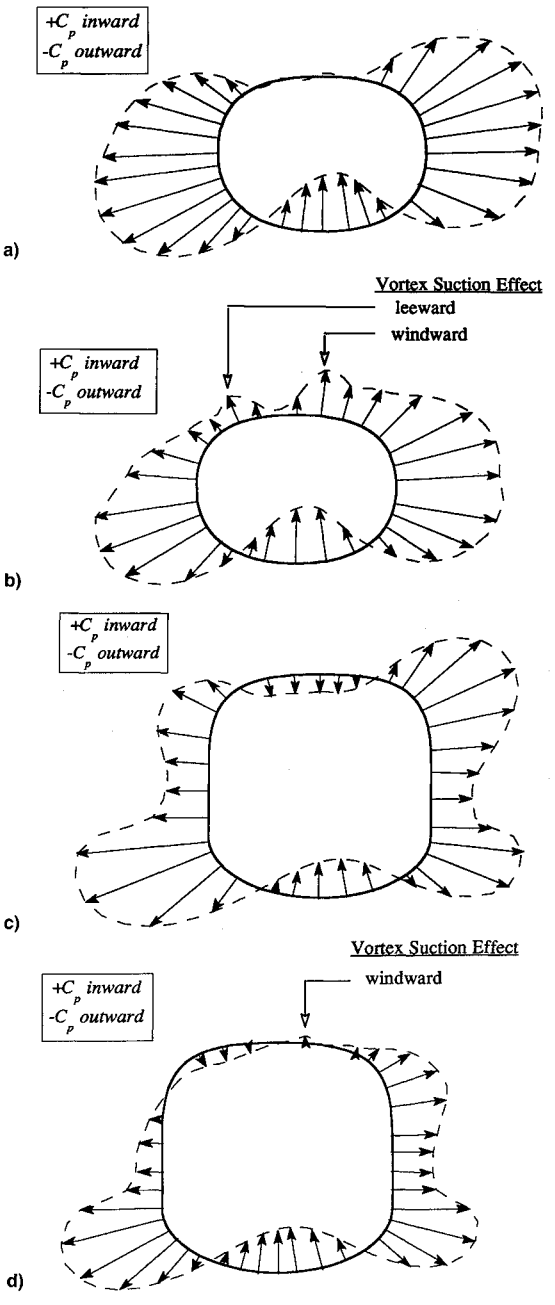

Fig. 11 F-5A surface pressure distribution visualization as normal vectors illustrating the contrast between inviscid and viscous flowfield predictions at FS 14.02 and FS 29.61 for α = 40 deg, β = 5 deg: a) inviscid prediction at FS 14.02, b) viscous prediction at FS 14.02, c) inviscid prediction at FS 29.61, and d) viscous prediction at FS 29.61.

$C_{n\beta}$. The inviscid computations took approximately 0.55 h of CPU time for convergence, and the turbulent computations took approximately 4.5 h to reduce oscillations in the lift and yawing moment coefficients to a negligible level.

Convergence histories for typical inviscid and viscous cases are given in Fig. 6. The convergence histories include the residual and the yawing moment coefficient. The inviscid calculations demonstrate strong convergence. Unlike the inviscid case, the turbulent computations show low-frequency decaying oscillations in values of C_L and C_n, and require over 5000 iterations to obtain a fully converged solution, where the directional stability shows no further change with iteration. The weak convergence of the residual is not unusual for this code. A discussion has been given by Hartwich and Frink.[21] In this case the introduction of periodic boundary conditions contributed to the decrease in convergence rate. The yawing moment history in Fig. 6b provided a much better indication of convergence to a steady-state solution than the residual.

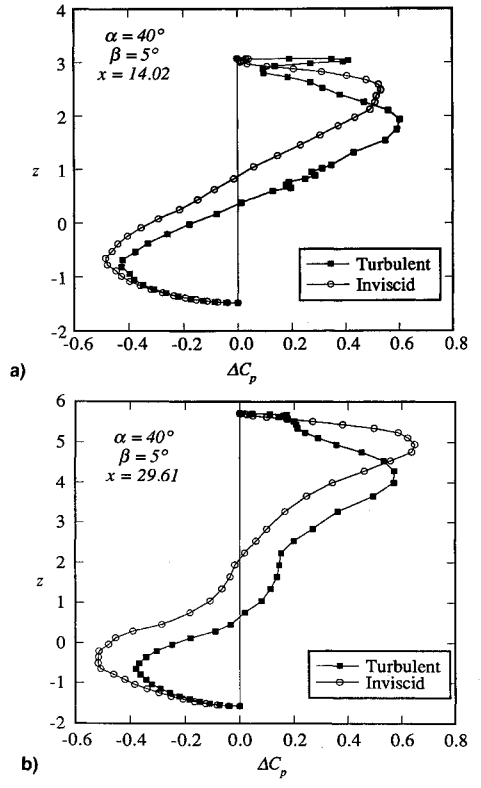

Fig. 12 Variation of ΔC_p vertically along cross section: a) FS 14.02 and b) FS 29.61.

Force Results

The F-5A forebody experimental directional stability data[4] are shown along with the computed inviscid and viscous results in Fig. 7. The computed values of $C_{n\beta}$ were obtained by a finite difference of the yawing moment coefficient C_n at β = 5 deg. The computed results show the same trend found in the wind-tunnel data. The inviscid results also indicate a slight tendency toward the stabilizing effect at high angles of attack, although to a much lesser degree, and don't agree with the data.

The results of the grid refinement study for both inviscid and viscous calculations are also shown for α = 40 deg. Some grid sensitivity was observed. Although the results changed slightly with grid resolution, the trends were the same in both cases. It was not possible to compute each α at the increased resolution, and the objective of our study was achieved with the basic grid.

At low angles of attack (10 and 20 deg), the inviscid and viscous calculations agree with each other and the data. At α = 30 deg, the viscous computations continue to agree with the data. At the higher angles of attack (40 and 45 deg), differences begin to appear. Considering the use of the thin-layer approximation, the state of development of turbulence models for massively separated flows, and the slight grid resolution effects, the agreement is surprisingly good. The viscous calculation results establish the effectiveness of a code like CFL3D in computing the directional stability characteristics for forebodies at high angles of attack.

Figure 8 shows the axial distribution of the side force contributing to the yawing moment presented above at one angle of attack (40 deg). The importance of the viscosity in producing positive stability is clearly demonstrated. Near the tip, the side force is a "drag" in the crossflow plane. However, the viscous solution develops a significant restoring force, with a positive side force over most of the forebody and increasing with downstream distance. This is a consequence of the increasing asymmetry of the forebody vortices with distance from the nose. The inviscid solution shows essentially no side force over the majority of the forebody.

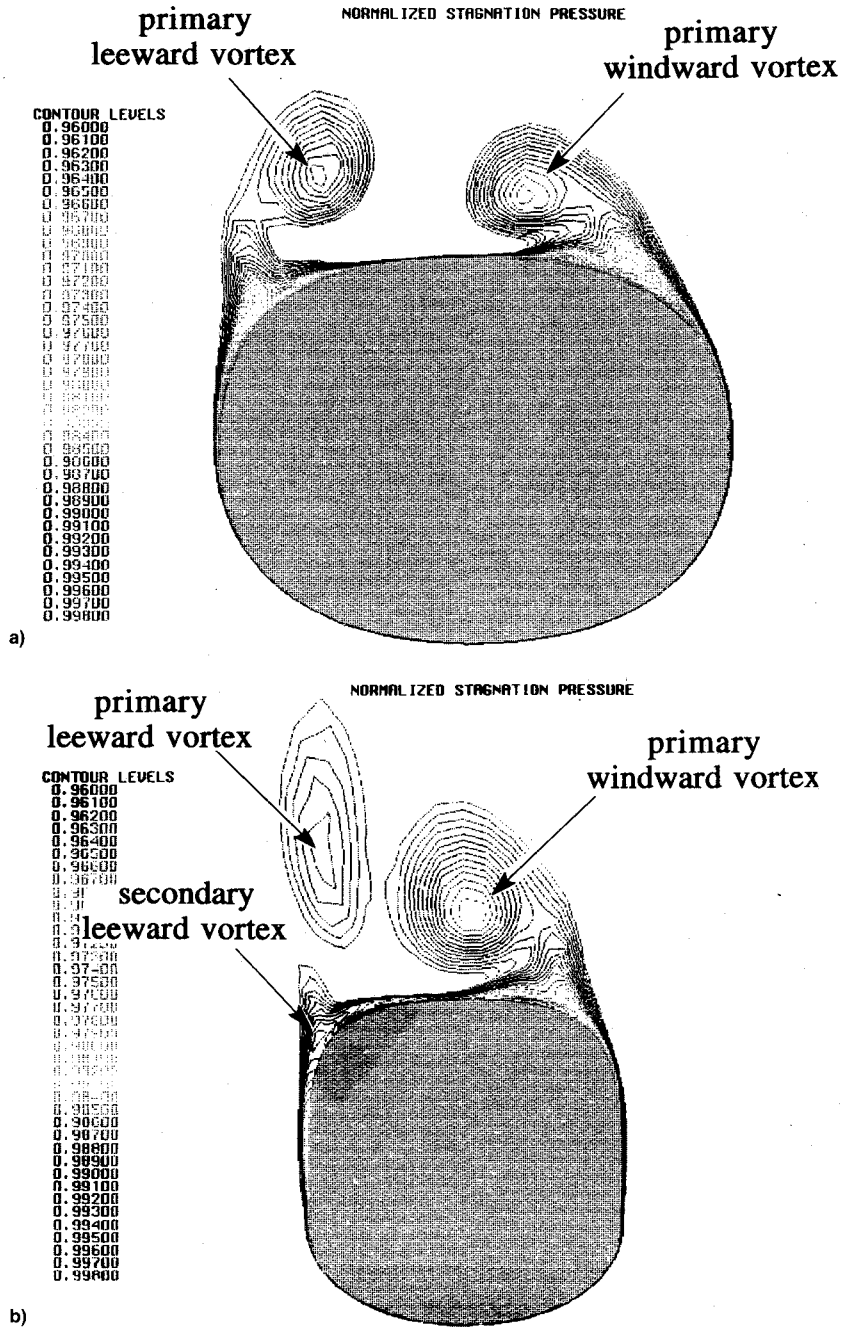

Fig. 13 F-5A flowfield stagnation pressure contours for α = 40 deg and β = 5 deg: a) FS 14.02 and b) FS 29.61.

Surface Pressure Distributions

Figures 9 and 10 show the circumferential pressure distribution at two stations for both inviscid and turbulent calculations. The corresponding cross-sectional shapes are shown at the bottom of the figures, and define the origin of the reference for the angular measure. The key features of interest on the pressure distributions are related to the surface location by the identifiers A–D. The results presented here were computed on the respective standard grids for the case of α = 40 deg and β = 5 deg, and clearly show the asymmetry in the pressure distributions due to sideslip.

The small negative suction peak pressures B and C in the viscous results in Fig. 9, FS 14.02, are due to the vortices just above the upper surface of the body. The lowest pressures, A and D, are actually inviscid in origin and are due to the acceleration of the crossflow around the body. At the aft station presented in Fig. 10, FS 29.61, the inviscid results contain distinct low-pressure peaks. These low-pressure regions are due to the acceleration of the crossflow around the highly curved sides of the body at this fuselage station. Considering the viscous solution at this station, the leeward vortex in the turbulent calculation is now far from the surface (shown later in Fig. 13b), and no explicit effect on the surface pressures can be identified. Point C identifies the suction pressure associated with the primary windward vortex. The flow is massively separated, with corresponding low-pressure gradients along the surface.

Figure 11 contains a normal vector representation of the surface pressure distribution around the two cross sections examined in Figs. 9 and 10. Vectors pointing out from the surface correspond to negative pressure coefficients (suction), and the vectors pointing inward correspond to positive pressure coefficients (higher pressures). Figures 11a and 11c present the predictions from the inviscid solution, and Figs. 11b and 11d present the viscous solution results. In each case, the crossflow stagnation pressure region is easily identified at the bottom of the figure.

Considering the inviscid results first, the pressure distributions are seen to expand smoothly around the sides of the body. The crossflow velocity is from the right, and there is a

slight asymmetry. At FS 14.02, the smooth cross section results in a smooth expansion and recompression. At FS 29.61, the emergence of distinct corners in the shape leads to separate low-pressure areas around the body.

The effects of viscosity can be studied by comparing Figs. 11b and 11d with their inviscid prediction counterparts. As expected, the character of the flow at the bottom of the cross section is nearly the same. At FS 14.02, the most notable difference is the effect of the vortex flow in the viscous solution, which produces the two low-pressure regions identified previously in Fig. 9. Also, the general magnitude of the suction is reduced on the top half of the cross section. At FS 29.61, the largest effect is the reduction of the strong pressure suction lobe in the inviscid solution at the top windward crossflow corner. Here, separation relieves the strong corner effect observed in the inviscid solution. The vortices are farther away from the surface, and their explicit effects are reduced.

Figure 12 contains the pressure differences ΔC_p between the two sides of the body for the pressure distributions at the stations shown in Figs. 9–11. The differences are presented along a vertical axis to provide insight into the distribution of side force at a particular station to help understand the effect of viscosity in creating the restoring force. Although the viscous effects are primarily associated with the vortex and separated flowfield on the top side of the forebody (shown in the next section), the effects of viscosity are seen to alter the balance of pressures between the sides of the body over most of the side projection. It is particularly interesting to notice that the near-zero side force associated with the inviscid flow arises as a delicate balance between a side force in one direction on the lower portion of the body, and a side force in the other direction on the upper part of the body. The effects of viscosity are to reduce the magnitudes of the peak effects, as well as producing a shift in the location of ΔC_p curve which results in a distribution which has a much larger net side force.

Flowfield Results

Figures 13a and 13b show the cross-sectional stagnation pressure contours at FS 14.02 and FS 29.61 for the viscous calculation at the same flow conditions shown in Figs. 9–12 (α = 40 deg and β = 5 deg). The vortex pattern and asymmetry are clearly seen here. The leeward vortex is farther away from the surface than the windward vortex. The asymmetry of the low surface pressures on the body under the vortices are generally considered to be acting to "pull" the body back to smaller sideslip, and thus provides a stabilizing moment. However, we have shown in Fig. 12 that the side force is affected by the separated flow indirectly through its affect on the pressure distribution over virtually the entire surface.

Conclusions

In this study a Navier-Stokes code has been used to simulate the aerodynamics of forebodies at combined angle of attack and sideslip. The F-5A forebody directional stability experimental results have been obtained computationally. By comparing inviscid and viscous computational solutions, the role of viscosity in creating the stabilizing effect of the forebody has been explicitly identified. An analysis of the force distribution on the body has been used to quantitatively identify the origins of the stabilizing effects of viscosity. This is the first time that the computation of directional stability of the forebody has been presented for one of the most significant wind-tunnel tests in high angle-of-attack aerodynamics. It provides an important demonstration of the capability of CFD to contribute to high angle-of-attack configuration design.

Acknowledgments

This analysis was made as part of the work conducted under NASA Grant NAG-1-1037. The results were obtained with the help of many people. At NASA Langley, Ed Waggoner supported the initiation of this work, Sue Grafton provided us with the forebody from the wind-tunnel model of the F-5A, Gary Erickson helped us contact Northrop, and James Luckring, Robert Hall, and Farhad Ghaffari each helped us do the work. At Northrop, Tom Heglund provided us with detailed F-5A lofting information. At Virginia Polytechnic Institute and State University, Robert Walters consulted with us regularly on the use of CFL3D, William McGrory provided us with his grid generator, and David Poteet made the F-5A forebody inspection. Each of these contributions is gratefully acknowledged.

References

[1]Chambers, J. R., "High-Angle-of-Attack Aerodynamics: Lessons Learned," AIAA Paper 86-1774, June 1986.

[2]Chambers, J. R., and Grafton, S. B., "Aerodynamic Characteristics of Airplanes at High Angle-of-Attack," NASA TM 74097, Dec. 1977.

[3]Rao, D. M., and Murri, D. G., "Exploratory Investigation of Deflectable Forebody Strakes for High Angle-of-Attack Yaw Control," AIAA Paper 86-0333, Jan. 1986.

[4]Grafton, S. B., Chambers, J. R., and Coe, P. L., Jr., "Wind-Tunnel Free-Flight Investigation of a Model of a Spin Resistant Fighter Configuration," NASA TN D-7716, June 1974.

[5]Ghaffari, F., Luckring, J. M., Thomas, J. L., and Bates, B. L., "Navier-Stokes Solutions about F/A-18 Forebody—LEX Configuration," AIAA Paper 89-0338, Jan. 1989.

[6]Hartwich, P. M., and Hall, R. M., "Navier-Stokes Solutions for Vortical Flows over a Tangent-Ogive Cylinder," *AIAA Journal*, Vol. 28, No. 7, 1990, pp. 1171–1179.

[7]Hartwich, P. M., Hall, R. M., and Hemsch, M. J., "Navier-Stokes Computations of Vortex Asymmetries Controlled by Small Surface Imperfections," *Journal of Spacecraft and Rockets*, Vol. 28, No. 2, 1991, pp. 258–264.

[8]Schiff, L. B., Degani, D., and Cummings, R. M., "Numerical Simulation of Separated and Vortical Flows on Bodies at Large Angles of Attack," *Numerical and Physical Aspects of Aerodynamic Flows*, Vol. IV, edited by T. Cebeci, Springer-Verlag, Berlin, 1990, pp. 205–222.

[9]Thomas, J. L., Van Leer, B., and Walters, R. W., "Implicit Flux-Split Schemes for the Euler Equations," AIAA Paper 85-1680, July 1985.

[10]Baldwin, B. S., and Lomax, H., "Thin Layer Approximation and Algebraic Model for Separated Turbulent Flows," AIAA Paper 78-257, Jan. 1978.

[11]Degani, D., and Schiff, L. B., "Computation of Supersonic Viscous Flows Around Pointed Bodies at Large Incidence," AIAA Paper 83-0034, Jan. 1983.

[12]Degani, D., and Schiff, L. B., "Computation of Turbulent Supersonic Flows Around Pointed Bodies Having Cross Flow Separation," *Journal of Computational Physics*, Vol. 66, Jan. 1986, pp. 173–196.

[13]Degani, D., Schiff, L. B., and Levy, Y., "Physical Considerations Governing Computation of Turbulent Flows over Bodies at Large Incidence," AIAA Paper 90-0096, Jan. 1990.

[14]Roe, P. L., "Characteristics Based Schemes for the Euler Equations," *Annual Review of Fluid Mechanics*, Vol. 18, 1986, pp. 337–365.

[15]Thomas, J. L., Walters, R. W., Reu, T., Ghaffari, F., Weston, R. P., and Luckring, J. M., "Application of a Patched-Grid Algorithm to the F/A-18 Forebody-Leading-Edge Extension Configuration," *Journal of Aircraft*, Vol. 27, No. 9, 1990, pp. 749–756.

[16]Walatka, P. P., Buning, P. G., Pierce, L., and Elson, A., "PLOT3D User's Manual," NASA TM 101067, March 1990.

[17]Liming, R. A., *Mathematics for Computer Graphics*, Aero Publishers, Fallbrook, CA, 1979.

[18]McGrory, W., private communication, Virginia Polytechnic Inst. and State Univ., Blacksburg, VA, June 1989.

[19]Walters, R. W., Reu, T., Thomas, J. L., and McGrory, W. D., "Zonal Techniques for Flowfield Simulation About Aircraft," *Computers & Structures*, Vol. 30, Nos. 1/2, 1988, pp. 47–54.

[20]Mason, W. H., and Ravi, R., "A Computational Study of the F-5A Forebody Emphasizing Directional Stability," AIAA Paper 91-3289, Sept. 1991.

[21]Hartwich, P. M., and Frink, N. T., "Estimation of Propulsion-Induced Effects on Transonic Flows over a Hypersonic Configuration," AIAA Paper 92-0523, Jan. 1992.